

# We are IntechOpen, the world's leading publisher of Open Access books Built by scientists, for scientists

4,800

Open access books available

122,000

International authors and editors

135M

Downloads

Our authors are among the

154

Countries delivered to

TOP 1%

most cited scientists

12.2%

Contributors from top 500 universities



WEB OF SCIENCE™

Selection of our books indexed in the Book Citation Index  
in Web of Science™ Core Collection (BKCI)

Interested in publishing with us?  
Contact [book.department@intechopen.com](mailto:book.department@intechopen.com)

Numbers displayed above are based on latest data collected.  
For more information visit [www.intechopen.com](http://www.intechopen.com)



## Robot vision using 3D TOF systems

Stephan Hussmann and Torsten Edeler  
*Westcoast University of Applied Sciences  
Germany*

### 1. Introduction

Consistent 3D imaging of robot surroundings is extremely useful for aiding navigation, and a lot of research effort has been applied to propose good solutions to this challenge. In principle there are three main methods used to acquire 3D information using vision-based systems: structure from motion (SfM) and stereo vision (SV) systems, laser range scanners (LRS) and time-of-flight (TOF) cameras.

SfM and SV systems usually rely on establishing correspondences between two images taken simultaneously (Faugeras, 1993), or taken by one camera at different times and places (Oliensis, 2000). Stereo cameras introduce physical restrictions on the robot due to the need for camera separation. Further, stereo cameras depend on texture matching from both camera images for range estimation. This produces a rather sparse and unevenly distributed data set. Due to the allocation problem dynamic tracking of objects is not an easy task (Hussmann & Liepert, 2009). SfM techniques must deal with correspondence, and also uncertainty about the position at which each image is taken, and dynamic changes that may occur in the time between the two images.

LRSs deliver one scanning line of accurate distance measurements often used for navigation tasks (Nuechter et al., 2003). LRSs measure distances at a coarse grid across the range sensor field-of-view, also providing sparse data sets. The major disadvantage of LRS systems is the use of mechanical components and that they do not deliver 3D range data at one image capture. In dynamical scenes the range data has to be corrected due to the laser scan process. They also do not deliver any intensity or colour information of the objects. Some researchers have mounted both LRS and camera on the same robot, and integrated the data to give both image and range information (Ho & Jarvis, 2008).

TOF cameras (Blanc et al., 2004 ; Schwarte et al., 1997) combine the advantage of active range sensors and camera based approaches as they provide a 2D image of intensity and exact (not estimated) distance values in real-time for each pixel. No data integration is needed since range and intensity measurements are made at each pixel. Compared to SV systems TOF cameras can deal with prominent parts of rooms such as walls, floors, and ceilings even if they are not structured. In addition to the 3D point cloud, contour and flow detection in the image plane yields motion information that can be used for applications such as car or person tracking (Hussmann et al., 2008). Compared to an LRS all range data are captured at one time between different object sample points. In conclusion it can be said

that TOF cameras are the most suitable 3D imaging systems for robot vision as they are able to deliver 3D dynamic information of objects.

Because of the enormous progress in TOF-vision systems, nowadays 3D matrix cameras can be manufactured and be used for many applications such as robotic, automotive, industrial, medical and multimedia applications. Due to the increasing demand of safety requirements in the automotive industry it can be assumed that the TOF-camera market will grow and the unit price of these systems in the mass production will drop down to ca. 100 € (Hussmann & Hess, 2006).

For all application areas new accurate and fast algorithms for 3D object recognition and classification are needed. As now commercial 3D-TOF cameras are available at a reasonable price the number of research projects is expected to increase significantly. One early example of using a TOF-camera based on the Photonic-Mixer-Devices (PMD)-Technology for 3D object recognition in TOF data sets are presented in (Hess et al., 2003). In this paper the transition from a general model of the system to specific applications such as intelligent airbag control and robot assistance in surgery are demonstrated. A more current example in using a PMD-TOF camera on a robot system, highlighting the advantages of TOF- compared to SV-vision systems, is reported in (Hussmann & Liepert, 2009).

This book chapter is structured as follows. In Section II we derive the basics of PMD TOF vision systems and expose the issues which motivate a new approach for robot vision systems. In Section III one exemplary robot application demonstrates the advantage of 3D-TOF vision systems based on the PMD-technology over the other vision-based systems. Concluding remarks will summarize the paper.

## 2. Basics of PMD TOF vision systems

### 2.1 Operating principle

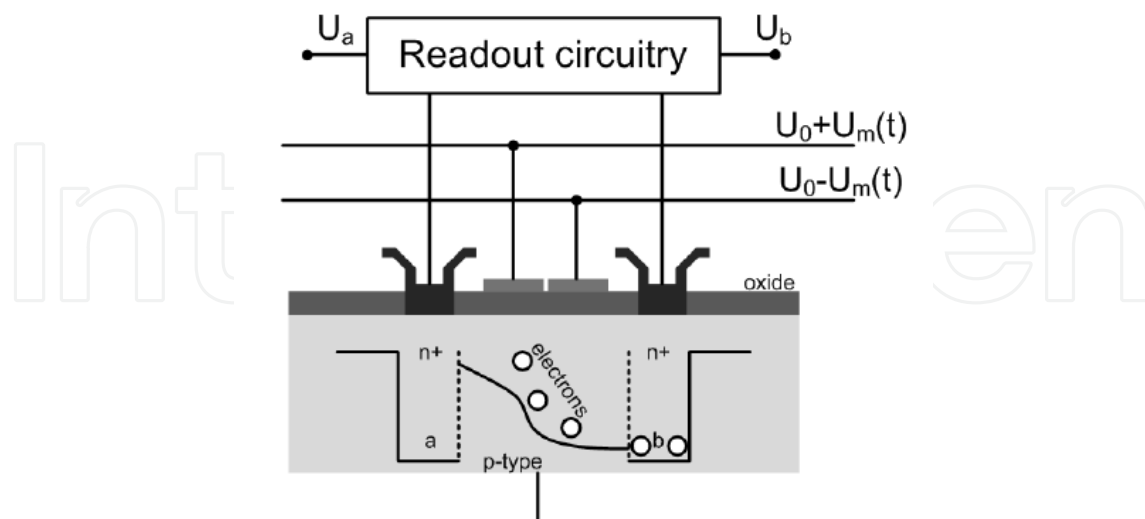


Fig. 1. Cross section of a typical PMD pixel

Fig. 1 shows the cross section of a typical PMD pixel comprising two symmetrical, transparent photo gates. These gates are the optical input window for the receiving

modulated optical echo  $P_{opt}$ . They are isolated from the p-doped substrate by a  $\text{SiO}_2$  - or  $\text{Si}_3\text{N}_4$  - isolation layer (channel stop) and bounded on the left and right side by  $n^+$  - diffusion readout gates. The photo gates are controlled by the modulation voltage  $u_m$  and the offset voltage  $U_0$ . The schematic potential distribution in the p-doped substrate between the photo gates is shown in Fig. 1 for a negative modulation voltage  $u_m$ .

A PMD pixel may be understood as a modulation controlled photo charge distributor (photonic mixer). In principle the PMD pixel works like a seesaw for electrons while controlling its motion by means of polarity and slope of the seesaw. If no modulated light is received the photo generated charges symmetrically drift to both readout gates  $a$  and  $b$ . If modulated light is received the photo generated charges drift only to readout gate  $b$ , when the modulated light and the modulation voltage have a phase difference of  $180^\circ$  (see Fig. 1). If the phase difference is  $0^\circ$  the photo generated charges drift only to readout gate  $a$ .

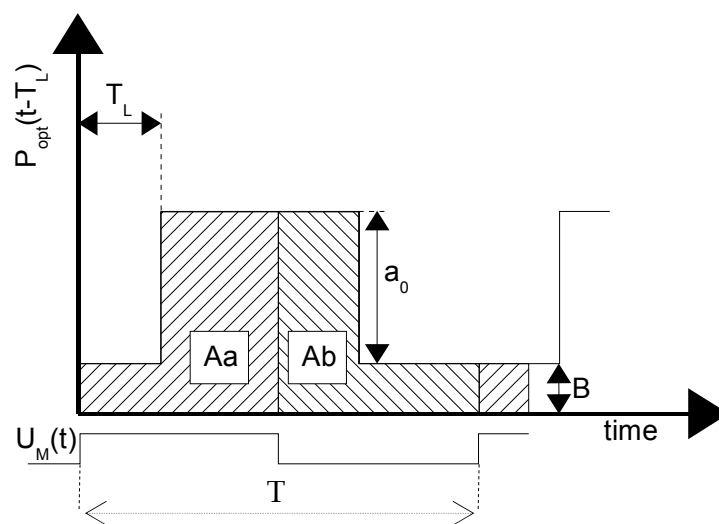


Fig. 2. Correlation process between the received optical echo  $P_{opt}$  and the modulation voltage  $u_m$  for one single modulation period

The readout gates  $a$  and  $b$  are each connected to an integration capacitor. Hence the corresponding voltages  $U_a$  and  $U_b$  can be expressed as a correlation function between the optical echo  $P_{opt}(t-T_L)$  and the modulation voltage  $u_m(t)$  over the integration time  $T_{int}$ . State of the art is to use continuous wave (CW) modulation with square waves for TOF cameras with a typical modulation frequency of 20 MHz. Hence the modulation voltage can be easily generated digitally with a high accuracy and stability using programmable logic devices (PLDs) such as complex programmable logic devices (CPLD) or field programmable gate arrays (FPGA) (Husmann et al., 2008).

Fig. 2 illustrates the correlation process for one single modulation period  $T$  for the two square waves  $P_{opt}(t-T_L)$  and  $u_m(t)$ . The modulation voltage  $u_m(t)$  is defined as follows:

$$u_m(t) = \begin{cases} 1, & \text{for } 0 \leq t - N \cdot T \leq T/2 \\ 0, & \text{for } T/2 < t - N \cdot T \leq T \end{cases}, \quad N = 0,1,2,\dots \quad (1)$$

$T_L$  is the 'time-of-flight' time for the light (camera-object-camera),  $B$  is the received unmodulated background light and  $a_0$  is the amplitude of the received modulated light.  $U_a$  and  $U_b$  are then proportional to the areas  $A_a$  and  $A_b$  as shown in Fig. 2. If the complete integration time  $T_{int}$  (corresponds to several hundreds or thousands of periods) has taken into account,  $U_a$  and  $U_b$  can be written as:

$$U_a(T_L) = K \cdot \int_0^{T_{int}} P_{opt}(t - T_L) \cdot u_m(t) dt = K \cdot \frac{T_{int}}{T} \cdot A_a(T_L) \quad (2)$$

and

$$U_b(T_L) = K \cdot \int_0^{T_{int}} P_{opt}(t - T_L) \cdot u_m(t - T/2) dt = K \cdot \frac{T_{int}}{T} \cdot A_b(T_L) \quad (3)$$

The conversion gain  $K$  converts the received optical energy into a voltage. The integration time  $T_{int}$  does not have to be necessarily a multiple of the single period time  $T$  as the number of periods integrated over the integration time is in the range of hundreds to thousands. Looking at Fig. 2 it can be noticed that  $U_a$  and  $U_b$  are always a positive voltage. To remove the influence of the background light the difference of  $\Delta U_{ab}$  has to be determined:

$$\Delta U_{ab}(T_L) = U_a - U_b = K \cdot \frac{T_{int}}{T} \cdot (A_a(T_L) - A_b(T_L)) \quad (4)$$

$\Delta U_{ab}$  relates to the distance value of a PMD pixel. The sum of  $U_a$  and  $U_b$  corresponds to all received and converted photons. Hence this sum is equivalent to the grey level value of standard CCD/CMOS video cameras:

$$\Sigma U_{ab} = U_a + U_b = K \cdot \frac{T_{int}}{T} \cdot (A_a + A_b) = K \cdot \int_0^{T_{int}} P_{opt}(t - T_L) dt \quad (5)$$

Equation (4) and (5) demonstrate the advantage of the PMD technology compared to other range measurement systems such as SV systems or LRS. The PMD pixel is a TOF vision system with inherent suppression of uncorrelated light signals such as sun light or other modulated light disturbances. More advantages of a PMD TOF vision system are the acquisition of the grey level and range data in each pixel without high computational cost and any moving components as well as the monocular setup.

## 2.2 Range image calculation

As mention in the last section the range value corresponds to  $\Delta U_{ab}$ . First the 'time-of-flight' time for the light  $T_L$  has to be determined. Two different solutions for equation (4) are needed to find  $T_L$ . Looking at Fig. 2 a mathematical description for  $U_a$  and  $U_b$  can be derived. Two cases have to be taken into account to determine the mathematical description.  $U_{a1}$  and  $U_{b1}$  are as follows for the first case ( $0 \leq T_L < T/2$ ):

$$U_{a1}(T_L) = K \cdot \frac{T_{\text{int}}}{T} \cdot \left[ B \cdot \frac{T}{2} + a_0 \cdot \left( \frac{T}{2} - T_L \right) \right] \quad \text{for } 0 \leq T_L < T/2 \quad (6)$$

and

$$U_{b1}(T_L) = K \cdot \frac{T_{\text{int}}}{T} \cdot \left[ B \cdot \frac{T}{2} + a_0 \cdot T_L \right] \quad \text{for } 0 \leq T_L < T/2 \quad (7)$$

Now the  $\Delta U_{ab1}$  can be calculated:

$$\Delta U_{ab1}(T_L) = K \cdot \frac{T_{\text{int}}}{T} \cdot a_0 \cdot \left[ \frac{T}{2} - 2T_L \right] \quad \text{for } 0 \leq T_L < T/2 \quad (8)$$

$U_{a2}$  and  $U_{b2}$  are as follows for the second case ( $T/2 \leq T_L \leq T$ ):

$$U_{a2}(T_L) = K \cdot \frac{T_{\text{int}}}{T} \cdot \left[ B \cdot \frac{T}{2} + a_0 \cdot \left( T_L - \frac{T}{2} \right) \right] \quad \text{for } T/2 \leq T_L \leq T \quad (9)$$

and

$$U_{b2}(T_L) = K \cdot \frac{T_{\text{int}}}{T} \cdot \left[ B \cdot \frac{T}{2} + a_0 \cdot (T - T_L) \right] \quad \text{for } T/2 \leq T_L \leq T \quad (10)$$

The corresponding  $\Delta U_{ab2}$  is then:

$$\Delta U_{ab2}(T_L) = K \cdot \frac{T_{\text{int}}}{T} \cdot a_0 \cdot \left[ -\frac{3}{2}T + 2T_L \right] \quad \text{for } T/2 \leq T_L \leq T \quad (11)$$

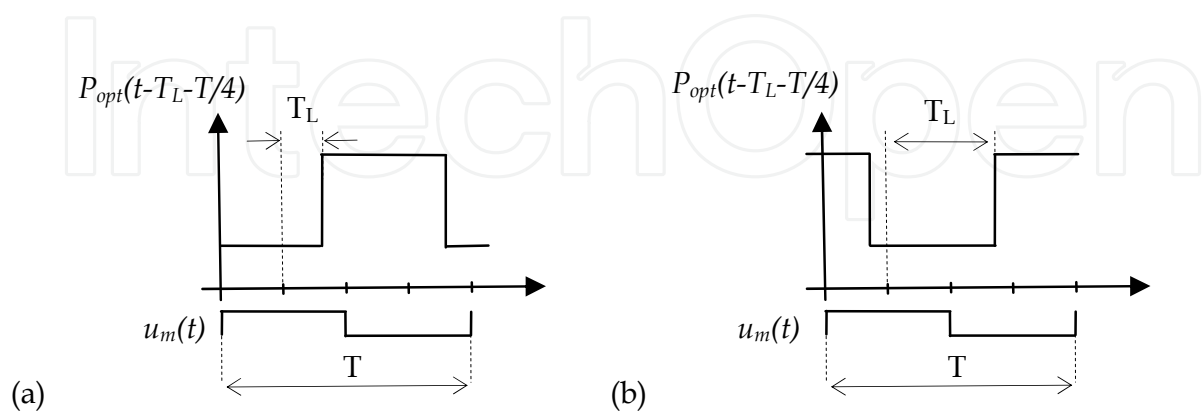


Fig. 3. Correlation process between the shifted optical echo and the modulation voltage for one single modulation period for (a)  $0 \leq T_L < T/4$  as well as  $3T/4 < T_L \leq T$  and (b)  $T/4 \leq T_L \leq 3T/4$

To get another solution for  $\Delta U_{ab}$  the optical echo  $P_{opt}(t-T_L)$  is shifted by  $T/4$ . Three cases have to be taken into account to determine a mathematical description for  $U_a$  and  $U_b$  as shown in Fig. 3.  $U_{a1}(T_L-T/4)$  and  $U_{b1}(T_L-T/4)$  are as follows for the first case ( $0 \leq T_L < T/4$ ):

$$U_{a1}(T_L - T/4) = K \cdot \frac{T_{int}}{T} \cdot \left[ B \cdot \frac{T}{2} + a_0 \cdot \left( \frac{T}{4} - T_L \right) \right] \quad \text{for } 0 \leq T_L < T/4 \quad (12)$$

and

$$U_{b1}(T_L - T/4) = K \cdot \frac{T_{int}}{T} \cdot \left[ B \cdot \frac{T}{2} + a_0 \cdot \left( \frac{T}{4} + T_L \right) \right] \quad \text{for } 0 \leq T_L < T/4 \quad (13)$$

The corresponding  $\Delta U_{ab1}(T_L-T/4)$  is then:

$$\Delta U_{ab1}(T_L - T/4) = -K \cdot \frac{T_{int}}{T} \cdot a_0 \cdot 2T_L \quad \text{for } 0 \leq T_L < T/4 \quad (14)$$

$U_{a2}(T_L-T/4)$  and  $U_{b2}(T_L-T/4)$  are as follows for the second case ( $T/4 \leq T_L \leq 3T/4$ ):

$$U_{a2}(T_L - T/4) = K \cdot \frac{T_{int}}{T} \cdot \left[ B \cdot \frac{T}{2} + a_0 \cdot \left( T_L - \frac{T}{4} \right) \right] \quad \text{for } T/4 \leq T_L \leq 3T/4 \quad (15)$$

and

$$U_{b2}(T_L - T/4) = K \cdot \frac{T_{int}}{T} \cdot \left[ B \cdot \frac{T}{2} + a_0 \cdot \left( \frac{3}{4}T - T_L \right) \right] \quad \text{for } T/4 \leq T_L \leq 3T/4 \quad (16)$$

The corresponding  $\Delta U_{ab2}(T_L-T/4)$  is then:

$$\Delta U_{ab2}(T_L - T/4) = K \cdot \frac{T_{int}}{T} \cdot a_0 \cdot [2T_L - T] \quad \text{for } T/4 \leq T_L \leq 3T/4 \quad (17)$$

$U_{a3}(T_L-T/4)$  and  $U_{b3}(T_L-T/4)$  are as follows for the third case ( $3T/4 < T_L \leq T$ ):

$$U_{a3}(T_L - T/4) = K \cdot \frac{T_{int}}{T} \cdot \left[ B \cdot \frac{T}{2} + a_0 \cdot \left( \frac{5T}{4} - T_L \right) \right] \quad \text{for } 3T/4 < T_L \leq T \quad (18)$$

and

$$U_{b3}(T_L - T/4) = K \cdot \frac{T_{int}}{T} \cdot \left[ B \cdot \frac{T}{2} + a_0 \cdot \left( T_L - \frac{3}{4}T \right) \right] \quad \text{for } 3T/4 < T_L \leq T \quad (19)$$

The corresponding  $\Delta U_{ab3}(T_L - T/4)$  is then:

$$\Delta U_{ab3}(T_L - T/4) = K \cdot \frac{T_{\text{int}}}{T} \cdot a_0 \cdot [2T - 2T_L] \quad \text{for } 3T/4 < T_L \leq T \quad (20)$$

Now all equations are derived which are needed to calculate  $T_L$ . By dividing equation (8) by equation (14)  $T_L$  can be calculated as follows for  $0 \leq T_L < T/4$ :

$$T_L = \frac{T}{4} \cdot \frac{\Delta U_{ab1}(T_L - T/4)}{\Delta U_{ab1}(T_L - T/4) - \Delta U_{ab1}(T_L)} \quad \text{for } 0 \leq T_L < T/4 \quad (21)$$

By dividing equation (8) by equation (17)  $T_L$  can be calculated as follows for  $T/4 \leq T_L < T/2$ :

$$T_L = \frac{T}{4} \cdot \frac{\Delta U_{ab2}(T_L - T/4) + 2\Delta U_{ab1}(T_L)}{\Delta U_{ab2}(T_L - T/4) + \Delta U_{ab1}(T_L)} \quad \text{for } T/4 \leq T_L < T/2 \quad (22)$$

By dividing equation (11) by equation (17)  $T_L$  can be calculated as follows for  $T/2 \leq T_L < 3T/4$ :

$$T_L = \frac{T}{4} \cdot \frac{2\Delta U_{ab2}(T_L) - 3\Delta U_{ab2}(T_L - T/4)}{\Delta U_{ab2}(T_L) - \Delta U_{ab2}(T_L - T/4)} \quad \text{for } T/2 \leq T_L < 3T/4 \quad (23)$$

By dividing equation (11) by equation (20)  $T_L$  can be calculated as follows for  $3T/4 \leq T_L \leq T$ :

$$T_L = \frac{T}{4} \cdot \frac{4\Delta U_{ab2}(T_L) + 3\Delta U_{ab3}(T_L - T/4)}{\Delta U_{ab2}(T_L) + \Delta U_{ab3}(T_L - T/4)} \quad \text{for } 3T/4 \leq T_L \leq T \quad (24)$$

Looking at equation (21) - (24) it can be seen that  $T_L$  depends only on the difference voltage  $\Delta U_{ab}$ . The range value  $R$  can now be calculated by taken into account the modulation frequency  $f_{\text{mod}}$  and the physical constant for the speed of light  $c$  ( $3 \cdot 10^8$  m/s).

$$R = \frac{c}{2 \cdot f_{\text{mod}}} \cdot \left( \frac{\omega T_L}{2\pi} \right) \quad (25)$$

It has to be noticed that the range calculation is only valid for ideal square waves. Due to the low-pass characteristic of the IR-LEDs used for the illumination unit, the square waves' harmonics are attenuated for larger frequencies. This results in an optical output that gradually looks sinusoidal for frequencies larger than 5-10 MHz. If this has to taken into account the range calculation has to be derived in a different way as shown in (Hussmann et al., 2008).



### 2.3 Amplitude and grey level image calculation

By subtracting equation (14) from equation (8) the modulation amplitude  $a_0$  can be determined for  $0 \leq T_L < T/4$ :

$$a_0 = \frac{2}{K \cdot T_{\text{int}}} \cdot (\Delta U_{ab1}(T_L) - \Delta U_{ab1}(T_L - T/4)) \quad (26)$$

By adding equation (17) and equation (8) the modulation amplitude  $a_0$  is as follows for  $T/4 \leq T_L < T/2$ :

$$a_0 = -\frac{2}{K \cdot T_{\text{int}}} \cdot (\Delta U_{ab1}(T_L) + \Delta U_{ab2}(T_L - T/4)) \quad (27)$$

By subtracting equation (17) from equation (11) the modulation amplitude  $a_0$  is as follows for  $T/2 \leq T_L < 3T/4$ :

$$a_0 = \frac{2}{K \cdot T_{\text{int}}} \cdot (\Delta U_{ab2}(T_L - T/4) - \Delta U_{ab2}(T_L)) \quad (28)$$

By adding equation (20) and equation (11) the modulation amplitude  $a_0$  is as follows for  $3T/4 \leq T_L \leq T$ :

$$a_0 = \frac{2}{K \cdot T_{\text{int}}} \cdot (\Delta U_{ab2}(T_L) + \Delta U_{ab3}(T_L - T/4)) \quad (29)$$

The gray level value of the PMD pixel, which is equivalent to the grey level value of standard CCD/CMOS video cameras, can be calculated by adding  $U_a$  and  $U_b$  as mentioned in section 2.1. It does not matter if equation (6) and (7) or equation (9) and (10) or equation (12) and (13) or equation (15) and (16) or equation (18) and (19) is used. The sum is always the same:

$$\Sigma U_{ab} = B \cdot T + \frac{T}{2} a_0 \quad (30)$$

The background light  $B$  can also easily be calculated using equation (26) - (30). By inserting equation (26) in equation (30) the background light  $B$  is for  $0 \leq T_L < T/4$ :

$$B = \frac{\Sigma U_{ab}}{T} + \frac{\Delta U_{ab1}(T_L - T/4) - \Delta U_{ab1}(T_L)}{K \cdot T_{\text{int}}} \quad (31)$$

By inserting equation (27) in equation (30) the background light  $B$  is for  $T/4 \leq T_L < T/2$ :

$$B = \frac{\Sigma U_{ab}}{T} + \frac{\Delta U_{ab2}(T_L - T/4) + \Delta U_{ab1}(T_L)}{K \cdot T_{\text{int}}} \quad (32)$$

By inserting equation (28) in equation (30) the background light  $B$  is for  $T/2 \leq T_L < 3T/4$ :

$$B = \frac{\Sigma U_{ab}}{T} + \frac{\Delta U_{ab2}(T_L) - \Delta U_{ab2}(T_L - T/4)}{K \cdot T_{\text{int}}} \quad (33)$$

By inserting equation (29) in equation (30) the background light  $B$  is for  $3T/4 \leq T_L \leq T$ :

$$B = \frac{\Sigma U_{ab}}{T} - \frac{\Delta U_{ab2}(T_L) + \Delta U_{ab3}(T_L - T/4)}{K \cdot T_{\text{int}}} \quad (34)$$

Again equation (26) - (29) demonstrate the advantage of the PMD technology compared to other range measurement systems such as SV systems or LRS. Using the amplitude image uncorrelated light signals such as sun light or other modulated light sources are suppressed. Still the grey level image ( $\Sigma U_{ab}$ ), which is normally used in 2D image processing applications with standard video cameras, is available. Hence standard 2D-Image processing algorithms can be used. The additional range values can lead to a superior solution for a given application based on 3D-TOF systems as demonstrated in the next section.

### 3. Robot application

#### 3.1 Experimental setup

To demonstrate the advantage of using 3D-TOF vision systems for robot applications compared to the other vision-based systems, the following laboratory setup has been chosen. The setup, shown in Fig. 4, demonstrates a real world problem on a smaller scale. A container ship has to be loaded in such a way that the containers use minimum storage area. A 3D-TOF camera (PMD[vision]® 19k) is mounted on top of the robot system, delivering the range data of the measure objects (containers) for the robot system (Kuka KR3). The robot system has a repeatability accuracy of  $\pm 0.05$  mm. A PC converts these range values in 3D space coordinates of the robot system and sends the range values, the centre of gravity (COG) values and rotation angle of the objects to the Kuka Robot. Subsequently the Kuka robot picks up the containers and places them optimally on the ship.



Fig. 4. Laboratory setup

### 3.2 System calibration

The 3D space coordinates of the measure objects are calculated using standard image segmentation and shape description methods. Before determining the 3D space coordinates, an  $x$ ,  $y$  and  $z$ -calibration of the range values of the 3D-TOF camera must be realized. For the  $x$ - and  $y$ -calibration the calibration technique proposed by Tsai is used (Tsai, 1987). For the  $z$ -calibration a linear calibration technique with respect to the background and the upper limit of the measuring range is used.

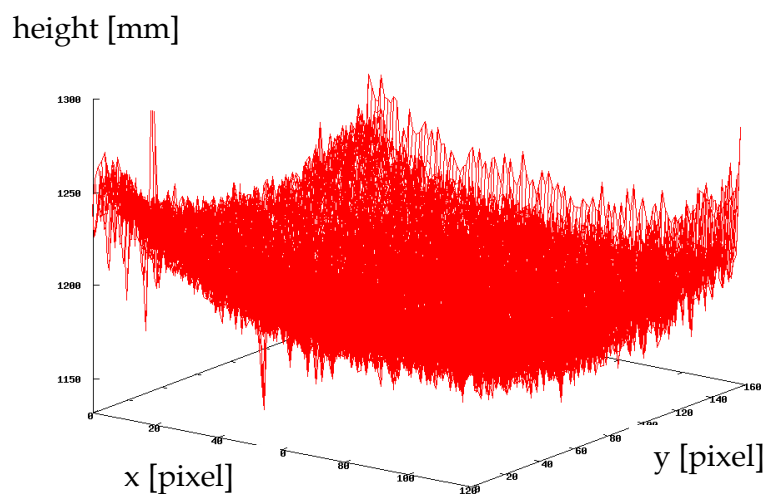


Fig. 5. Range image of a planar surface

Fig. 5. shows the range image of a planar surface. Due to the opening angle of the optics the outer pixel have a longer optical path therefore the range measurements are larger compared to the centre pixels. To correct this effect a background image is captured which is always subtracted from a taken range image. Hence for the range calibration first a range image of the background  $R_B$  is taken. This range image is taken at the beginning of the measuring range. In our application the wooden platform of the laboratory setup without the measure objects. Subsequently another range image  $R_x$  is taken at the end of the measuring range  $x$ . The corrected range value  $R_{cor}$  can then be calculated as follows:

$$R_{cor} = \frac{R - R_B}{R_x - R_B} \cdot x \quad (35)$$

It has to be noticed that the measuring range in this application is very small (around 10 cm). A more sophisticated calibration method has to be used for longer measuring ranges.

### 3.3 Image segmentation and object analysis algorithms

A 4-connected chain code algorithm is used to extract the measure objects. Chain codes can also be used to calculate certain boundary features such as object perimeter, width and height (Pitas, 2000). In this application the chain codes are used to segment the objects in the range image of the 3D-TOF camera and to place a surrounding rectangle. The compression advantage is not applied because the object boundary coordinates are needed for determining the surrounding rectangle. Once each measure object is segmented by its surrounding rectangle in the range image, the content of the rectangle is binaries into background and object.

Fig. 6 shows a screenshot of the developed graphical user interface (GUI) of the robot application. In the upper left corner the range image of the background  $R_B$  is shown. It can be clearly seen that the range measurements of the outer pixel are larger compared to the centre pixels (a brighter colour means a smaller range value). Beside the background range image is the grey level image of the scene. A segmentation of the objects is difficult as the objects have the same grey level values as the background (wooden objects on a wooden platform). The grey level histogram in the lower right corner in Fig. 6 illustrates this circumstance. The object grey level values can not be separated from the background grey level values.

The image beside the grey level image shows the uncorrected range image of the scene. Again it can be noticed that the range measurements of the outer pixel are larger compared to the centre pixels. The last image in the row (upper right corner) shows the result of the subtraction (range image - background range image). The objects can now easily be detected in the range image. Applying the image segmentation and object analysis algorithms leads to the last image shown in the lower right corner. All objects are segmented by their surrounding rectangles and can be separately chosen by the software. The COG is illustrated by the blue cross and the rotation angle by the white dotted line.

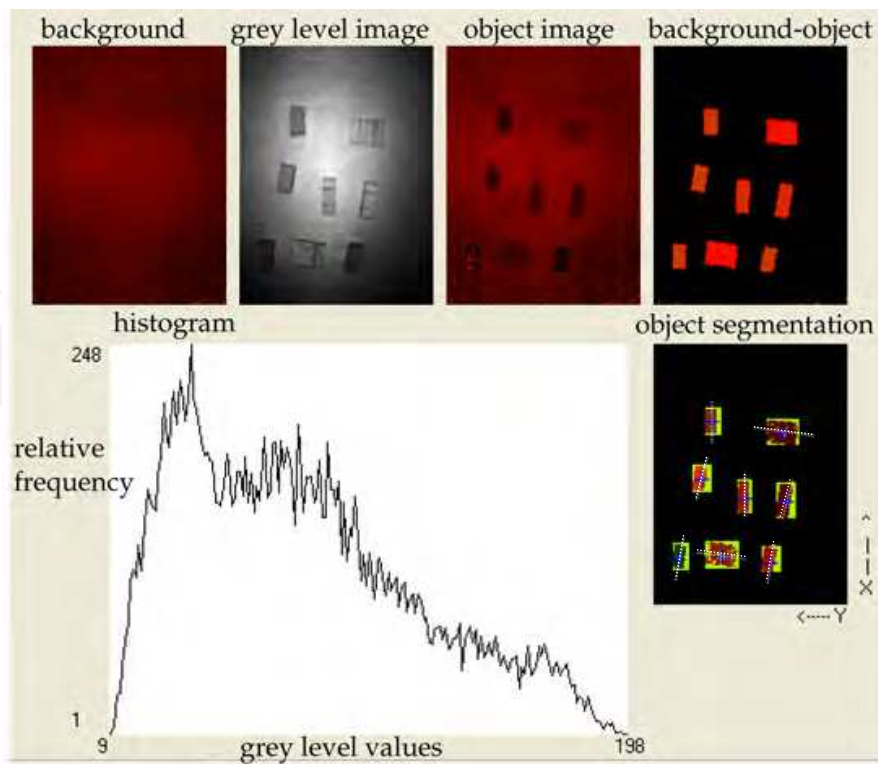


Fig. 6. Screen shot of the robot application GUI showing the grey level histogram

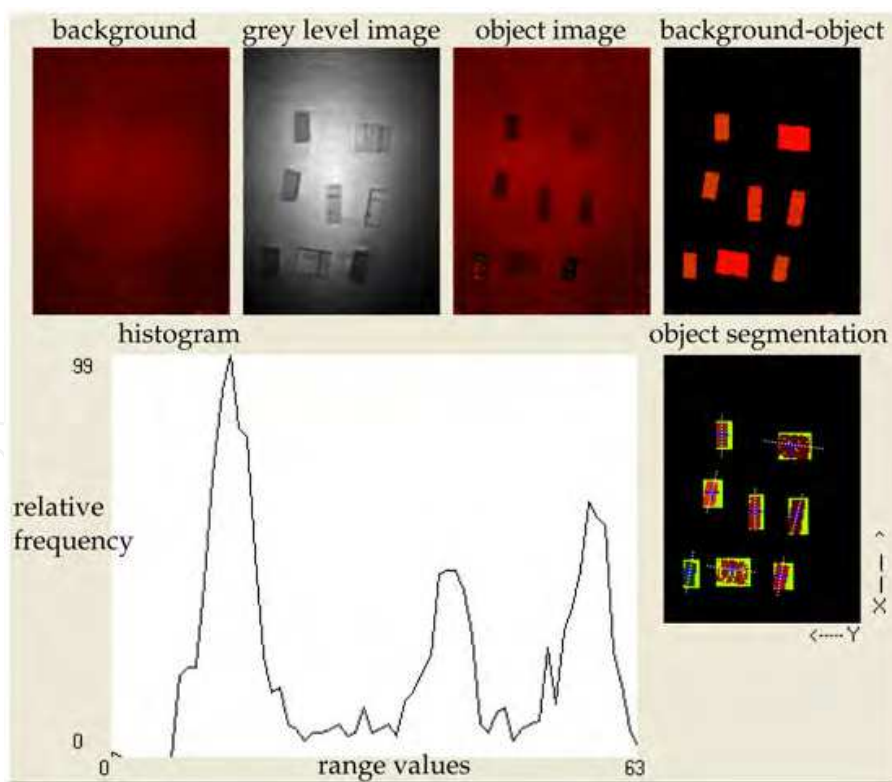


Fig. 7. Screen shot of the robot application GUI showing the range histogram

The only difference between Fig. 6 and Fig. 7 is the image in the lower left corner. The image shows the histogram of the range image. In comparison to the grey level histogram a segmentation of the object are now obvious. The three peaks illustrate the three different object heights (wooden block standing, on the side and on the other side). Fig. 6 and Fig. 7 make it clear that TOF vision system are superior in scenes with equal grey level values compared to the other vision based systems for robot applications. The object segmentation and analysis can be realized without complex image algorithms.

Subsequently the  $(x, y, z)$ -coordinates of the COG and the rotation angle of the objects are sent to the robot system. A more detailed algorithm description can be found in (Hussmann & Liepert, 2009). The Kuka K3 has now all required position data to pick up the containers correctly and place them on the ship

### 3.4 Experimental results

The experimental results show that the proposed TOF vision systems cannot only be used for long range measurements up to 7.5 m but also for near range measurements up to 1.2 m. The accuracy and repeatability of the system is applicable for industrial applications. The robot could pick up all measure objects correctly and placed them on the ship. Even when objects with different heights are placed in random positions on the table, the robot vision system worked fine. A more detailed description of the experimental results can be found in (Hussmann & Liepert, 2009).

## 4. Conclusion

In this chapter we highlighted the advantages of the PMD technology for robot vision compared to other range measurement systems such as SV systems or LRS. The equations needed for the design of such a system are derived and demonstrate the simplicity of the extraction of the range information. A PMD camera delivers absolute geometrical dimensions of objects without depending on the object surface, - distance, -rotation and - illumination. Hence PMD TOF vision systems are rotation-, translation- and illumination invariant.

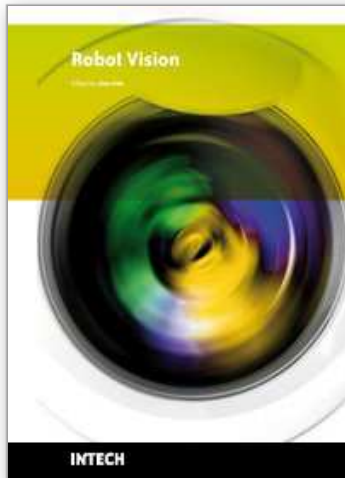
The major advantage of the PMD technology is the delivery of an evenly distributed range and intensity images because each pixel calculates a range and intensity value. The PMD technology has an inherent suppression of uncorrelated light signals such as sun light or other modulated light disturbances. However if those light sources saturate the sensor, the range information is lost. More advantages of a PMD technology are the acquisition of the intensity and range data in each pixel without high computational cost and any moving components as well as the monocular setup. All these advantages lead to a compact and economical design of 3D TOF vision system with a high frame rate. This vision system can not only be used for robot applications but also for many other applications such as automotive, industrial, medical and multimedia applications.

In this chapter experimental results of a PMD TOF vision system for a typical robot application are presented. The range data image of the 3D-TOF camera allows a correct segmentation of objects with equal gray level values. In such images, SV systems have difficulties to find corresponding image coordinates and therefore complex algorithms have to be used to get a correct object segmentation. The described application in this paper has demonstrated that a 3D-TOF robot vision system segments successfully objects with the

same gray level values as the background (wooden objects on a wooden platform). Furthermore it has been shown that the range data of the 3D-TOF camera is independent on the reflection coefficient of the measured objects. The reflection coefficient influences the received modulation amplitude and the modulation amplitude has no effect on the range measurement. The experimental results demonstrate that the accuracy and repeatability of the 3D-TOF robot vision system is applicable for industrial applications.

## 5. References

- Blanc, N., Oggier, T., Gruener, G., Weingarten, J., Codourey, A. & Seitz, P. (2004). Miniaturized smart cameras for 3D-imaging in real-time, *Proc. of the IEEE Sensors*, vol.1, pp. 471-4
- Faugeras, O. (1993). *Three-Dimensional Computer Vision: A Geometric Viewpoint*, MIT Press, Cambridge, Massachusetts
- Hess, H., Albrecht, M., Grothof, M., Hussmann, S., Oikonomidis, N. & Schwarte, R. (2003). 3D object recognition in TOF data sets, *Proc. SPIE*, vol. 5086, pp. 221-228
- Ho, N. & Jarvis, R. (2008). Towards a Platform Independent Real-Time Panoramic Vision Based Localisation System, *Proc. of the Australasian Conference on Robotics and Automation*, Canberra
- Hussmann, S. & Hess, H. (2006). Dreidimensionale Umwelterfassung, *Trade Journal: "Elektronik automotive"*, WEKA Publisher House, Issue 8, ISSN 1614-0125, pp. 55-59
- Hussmann, S., Ringbeck, T. & Hagebecker, B. (2008). A performance review of 3D TOF vision systems in comparison to stereo vision systems, In: *Stereo Vision* (Online book publication), I-Tech Education and Publishing, Vienna, Austria, ch. 7, ISBN 978-953-7619-22-0, pp. 103-120
- Hussmann, S. & Liepert, T. (2009). 3D-TOF Robot Vision System, *IEEE Trans. on Instrumentation and Measurement*, 58(1), pp.141-146
- Lange, R. & Seitz, P. (2001). Solid-state time-of-flight range camera, *IEEE Journal of Quantum Electronics*, vol. 37, no. 3, pp. 390-397
- Nuechter, A., Surmann, H. & Hertzberg, J. (2003). Automatic model refinement for 3D reconstruction with mobile robots, *Proc. of the 4<sup>th</sup> IEEE Intl. Conference on Recent Advances in 3D Digital Imaging and Modeling*, pp. 394-401
- Oliensis, J. (2000). A Critique of Structure-from-Motion Algorithms, *Computer Vision and Image Understanding*, 80(2), pp. 172-214
- Pitas, I. (2000). *Digital Image Processing Algorithms and Applications*, John Wiley & Sons, ISBN-0-471-37739-2
- Ringbeck, T. & Hagebecker, B. (2007). A 3D Time of flight camera for object detection, *Proc. of the 8th Conf. On Optical 3-D Measurement Techniques*, Zürich, Online-publication: (<http://www.pmdtec.com/inhalt/download/documents/070513Paper-PMD.pdf>)
- Schwarte, R., Xu, Z., Heinol, H., Olk, J., Klein, R., Buxbaum, B., Fischer H. & Schulte, J. (1997). New electro-optical mixing and correlating sensor: facilities and applications of the photonic mixer device (PMD), *Proc. SPIE*, vol. 3100, pp. 245-53
- Tsai, R. Y. (1987). A versatile Camera Calibration Technique for High-Accuracy 3D Machine Vision Metrology Using Off-the-Shelf TV Cameras and Lenses, *IEEE Journal of Robotics and Automation*, RA-3(4), pp. 323-44



## **Robot Vision**

Edited by Ales Ude

ISBN 978-953-307-077-3

Hard cover, 614 pages

**Publisher** InTech

**Published online** 01, March, 2010

**Published in print edition** March, 2010

The purpose of robot vision is to enable robots to perceive the external world in order to perform a large range of tasks such as navigation, visual servoing for object tracking and manipulation, object recognition and categorization, surveillance, and higher-level decision-making. Among different perceptual modalities, vision is arguably the most important one. It is therefore an essential building block of a cognitive robot. This book presents a snapshot of the wide variety of work in robot vision that is currently going on in different parts of the world.

### **How to reference**

In order to correctly reference this scholarly work, feel free to copy and paste the following:

Stephan Hussmann and Torsten Edeler (2010). Robot vision using 3D TOF systems, Robot Vision, Ales Ude (Ed.), ISBN: 978-953-307-077-3, InTech, Available from: <http://www.intechopen.com/books/robot-vision/robot-vision-using-3d-tof-systems>

**INTECH**  
open science | open minds

### **InTech Europe**

University Campus STeP Ri  
Slavka Krautzeka 83/A  
51000 Rijeka, Croatia  
Phone: +385 (51) 770 447  
Fax: +385 (51) 686 166  
[www.intechopen.com](http://www.intechopen.com)

### **InTech China**

Unit 405, Office Block, Hotel Equatorial Shanghai  
No.65, Yan An Road (West), Shanghai, 200040, China  
中国上海市延安西路65号上海国际贵都大饭店办公楼405单元  
Phone: +86-21-62489820  
Fax: +86-21-62489821



© 2010 The Author(s). Licensee IntechOpen. This chapter is distributed under the terms of the [Creative Commons Attribution-NonCommercial-ShareAlike-3.0 License](#), which permits use, distribution and reproduction for non-commercial purposes, provided the original is properly cited and derivative works building on this content are distributed under the same license.

IntechOpen

IntechOpen